Numerical study of stretched smectic-*A* elastomer sheets

A. W. Brown and J. M. Adams
SEPnet and the Department of Physics, Faculty of Engineering and Physical Sciences, University of Surrey, Guildford, GU2 7XH, United Kingdom
(Received 8 May 2013; published 30 July 2013)

We present a numerical study of stretching monodomain smectic-*A* elastomer sheets, computed using the finite element method. When stretched parallel to their smectic layer normal the smectic layers are unstable to a transition to a buckled state. We model macroscopic deformations by replacing the microscopic energy with a coarse grained effective free energy that accounts for the fine-scale layer buckling. We augment this model with a term to describe the energy of deforming buckled layers, which is necessary to reproduce the experimentally observed Poisson ratios postbuckling. We examine the spatial distribution of the microstructure phases for various stretching angles relative to the layer normal and for different length-to-width aspect ratios. When stretching parallel to the layer normal the majority of the sample forms a bidirectionally buckled microstructure, except at the clamps where a unidirectionally buckled microstructure is predicted. When stretching at small inclinations to the layer normal the phase of the sample is sensitive to the aspect ratio of the sample, with the bidirectionally buckled phase persistent to large angles only for small aspect ratios. We relate these theoretical results to experiments on smectic-*A* elastomers.

DOI: 10.1103/PhysRevE.88.012512 PACS number(s): 61.30.Vx, 83.80.Va, 46.32.+x, 02.70.Dh

I. INTRODUCTION

Liquid crystal elastomers (LCEs) are rubbery materials that are composed of liquid crystalline polymers (LCPs) cross-linked into a network. The rodlike mesogens incorporated into the LCPs have random orientations in the high-temperature isotropic phase, but can adopt the canonical liquid crystalline phases at lower temperatures. The liquid crystal phase of the mesogens plays a crucial role in the mechanical properties of the LCE. We will focus here on the smectic-*A* (Sm-*A*) phase, where the mesogens form a layered structure with the layer normal parallel to the molecular orientation as shown in Fig. 1.

In the absence of the polymer network, the layers of the liquid Sm-*A* phase are unstable to a buckling instability when strained parallel to their layer normal [1]. Models of layered materials, containing free energy penalties for layer curvature and layer dilation, exhibit layer buckling [2]. The models predict that just after the buckling threshold strain the layer modulation in a single direction is degenerate with bidirectional modulation. At larger strain this degeneracy is removed and bidirectional modulation is lower in energy. This theory of bidirectional buckling is consistent with experiments on liquid smectics, where two directions of buckling are observed in x-ray-scattering patterns [3]. The layer buckling is relaxed away in liquid smectics by the propagation of dislocations into the layers that relieve the strain. The smectic layer modulus in liquids is typically $B \approx 10^7$ Pa [3].

The first single-domain Sm-*A* elastomer was based on side chain liquid crystalline polymers (see Fig. 1) and reported by Nishikawa *et al*. [4]. A single domain was obtained by cross-linking the elastomer subjected to a uniaxial mechanical stress, which serves to align the layers and hence form an optically transparent elastomer. The sample remains transparent on stretching perpendicular to the layer normal and has Poisson ratios of $(0,1)$, indicating that the number of layers is preserved and that the deformation is accommodated within the layers. The modulus is of order $\mu \sim 10^5$ Pa for this deformation. The elastomer is initially much stiffer when stretched parallel to the layer normal, having the same modulus B as the liquid smectic and Poisson ratios of $(\frac{1}{2},\frac{1}{2})$. On stretching parallel to the layer normal their elastic modulus drops sharply to $\sim\mu$ above a threshold strain of a few percent, where the elastomer becomes cloudy [5]. The x-ray-scattering pattern indicates that the layers are buckled and the reduction in x-ray intensity shows that the modulation is in more than one direction as layers tilt out of the x-ray-scattering plane. Unlike the liquid smectic phase, the layer buckling cannot be relaxed away by the propagation of defects. More detailed x-ray studies of similar side-chain systems reveal that the layers behave as if they are embedded in the rubber matrix [6]. Later experiments on side-chain systems with different chemistry have shown the same threshold behavior, but the samples remain transparent throughout the deformation [7]. The behavior at the threshold has been shown to depend on the type of smectic ordering present [8] and on the degree of cross-linking in the elastomer [9]. Some side-chain systems show behavior closer to isotropic rubbers [10,11], thought to be caused by the interpenetration of smectic layers [12]. Here we will focus on the Nishikawa-type samples.

Smectic elastomers with a main chain polymer architecture (where the mesogens are incorporated directly into the backbone) have contrasting behavior to side-chain systems. The difference between the elastic moduli in the parallel and perpendicular directions is not as great and the x-ray-scattering patterns show increased ordering on stretching parallel to the layer normal [13]. It is thought that hairpin defects—sharp reversals in the chain orientation—play a crucial role in the softening behavior rather than layer buckling [13–15]. The smectic layers do not seem to be strongly coupled to the rubber matrix and hence do not behave as embedded planes. Experiments suggest that smectic layers in smectic-*C* main chain elastomers are also only weakly coupled to the rubber matrix [16].

Theoretical models of smectic elastomers have been successful in describing the mechanical behavior of

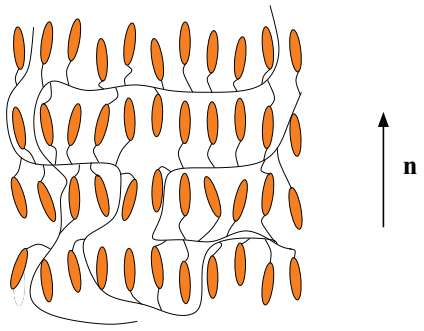

FIG. 1. (Color online) Illustration of the Sm-A phase in a side-chain LCE. The layer normal $\mathbf{n}$ is parallel to the molecular orientation.

side-chain systems. Phenomenological models developed using Lagrangian elasticity theory [17] and statistical physics [18] both describe the buckling behavior of smectic elastomers. These theories are equivalent for small strains once the strain-induced tilt of the director is included [19–21]. The buckling instability predicted by these models is symptomatic of a nonconvex free energy function. The free energy is minimized by a fine-scale mixture of deformations whose average is the macroscopic deformation. We will not resolve this microstructure, but will use a coarse grained Sm-A free energy based on the local deformation gradient only [22]. This model enables numerical computations of the deformation of a smectic elastomer to be carried out without modeling the microscopic length scale over which layer buckling occurs. Resolving the length scale of the microstructure would require the inclusion of spatial gradients in the deformation, for example, arising from Frank elastic energy. We will focus on using the coarse grained free energy model for realistic geometries of tensile loading of smectic elastomers that have been studied experimentally. A similar program has been successfully pursued for nematic elastomers, where the free energy density is also nonconvex. The resulting theoretical predictions of microstructure [23–25] are in good agreement with experiment [26,27].

For elastomers in the smectic-C phase there are several interesting features in the mechanical models, such as spontaneous deformations as observed in nematic elastomers [28,29]. While the set of all deformations that are zero energy (the quasiconvex hull) has been computed [30], the quasiconvex envelope has not, so it is not yet possible to carry out a numerical study as done here for the Sm-A phase.

II. MODEL

We will use the free energy density for a side-chain Sm-A elastomer derived in Ref. [18]. This has two contributions: the energetic cost of changing the smectic layer spacing and the entropic term from stretching the underlying polymer network. It contains parameters for the smectic layer modulus B, the rubber shear modulus μ, the polymer anisotropy r, and the reference state layer normal $\mathbf{n}_0$. By using the high-temperature isotropic state as the reference state this free energy density can be simplified as shown in Appendix A. It is also shown in Appendix A that the simplified free energy density can be approximated by the expression

$$W(\mathbf{F}) = \mathrm{Tr}(\mathbf{F}\cdot\mathbf{F}^T) + k(|\mathrm{cof}\,\mathbf{F}\cdot\mathbf{n}_0| - q)^2, \tag{1}$$

where $\mathbf{F} = \nabla\mathbf{y}$ is the deformation gradient, with $\mathbf{y}$ the displacement from the reference state, the cofactor of $\mathbf{F}$ is denoted $\mathrm{cof}\,\mathbf{F} = \mathbf{F}^{-T}$ (assuming $\det\mathbf{F} = 1$), and $W(\mathbf{F})$ has been made dimensionless by dividing the original free energy density by $\frac{1}{2}\mu r^{1/3}$ [22]. The first term in Eq. (1) is the entropic elasticity of the network and the second is the smectic layer compression term. We have disregarded an arbitrary additive constant and assumed that deformations are volume conserving, i.e., $\det\mathbf{F} = 1$, in deriving this expression. The constants q and k are given by

$$q = r^{-1/3}\left(1 + \frac{\mu}{B}(1-r)\right), \tag{2}$$

$$k = \frac{B}{\mu r^{2/3} q^3}. \tag{3}$$

The free energy density of Eq. (1) is not convex and so the free energy of a homogeneous deformation can be lowered by the formation microstructure, i.e., a spatial variation in the deformation gradient. Physically this microstructure corresponds to the buckling of the smectic layers. The quasiconvex envelope of $W(\mathbf{F})$ provides a coarse grained free energy density that is optimized over the possible microstructures and is given by

$$W^{qc}(\mathbf{F}) = \inf_{\mathbf{y}\in W_0^{1,\infty}} \left\{ \frac{1}{|\Omega|}\int_\Omega W(\mathbf{F}+\nabla\mathbf{y}(x))dx \right.$$
$$\left. : \mathbf{y}(x) = 0 \ \text{ on } \partial\Omega \right\}, \tag{4}$$

where Ω denotes the volume of the domain and $\partial\Omega$ denotes its boundary. An analytic expression for the quasiconvex envelope of Eq. (1) was derived in Ref. [22] and we summarize it here. To write an expression for $W^{qc}(\mathbf{F})$ we will need the largest singular value of the matrix $\mathbf{F}$ denoted by $\lambda_{\max}(\mathbf{F})$, i.e.,

$$\lambda_{\max}(\mathbf{F}) = \sup\{|\mathbf{F}\cdot\mathbf{e}| : \mathbf{e}\in\mathbb{R}^3, |\mathbf{e}| = 1\}. \tag{5}$$

For the Sm-A LCE model in Eq. (1) $W^{qc}(\mathbf{F})$ can be written in terms of the two convex functions of $\mathbf{F}$,

$$b = \lambda_{\max}(\mathbf{F}\cdot\mathbf{P})^2, \tag{6}$$

$$d = |\mathrm{cof}\,\mathbf{F}\cdot\mathbf{n}_0|, \tag{7}$$

where the matrix $\mathbf{P} = \mathbf{I} - \mathbf{n}_0\mathbf{n}_0^T$ projects out the $\mathbf{n}_0$ component

$$W^{qc}(\mathbf{F}) = \begin{cases} |\mathbf{F}\cdot\mathbf{n}_0|^2 + f(b,d), & \det\mathbf{F} = 1, \\ \infty & \text{otherwise}, \end{cases} \tag{8}$$

where

$$f(b,d) = \begin{cases} b + \frac{d^2}{b} + k(d-q)^2, & d \geqslant \frac{kqb}{kb+1} \\ b + \frac{kq^2}{kb+1}, & b \geqslant q - \frac{1}{k}, \quad d \leqslant \frac{kqb}{kb+1} \\ 2q - \frac{1}{k}, & b \leqslant q - \frac{1}{k}. \end{cases} \tag{9}$$

Equation (8) is a coarse grained model of a Sm-A elastomer that takes into account the formation of microstructure, without resolving the fine-scale oscillations in the deformation gradient.

A. Equilibrium

To compare with experimental results it is convenient to work with deformations relative to the low-temperature equilibrium Sm-A state. The system undergoes a volume conserving uniaxial deformation as it is cooled from the isotropic state to the smectic state. This uniaxial deformation along the layer normal minimizes Eq. (8). If we input the uniaxial deformation

$$\mathbf{F}_0 = \begin{pmatrix} 1/\lambda_0^2 & 0 & 0 \\ 0 & \lambda_0 & 0 \\ 0 & 0 & \lambda_0 \end{pmatrix} \tag{10}$$

into the total free energy $W^{qc}(\mathbf{F})$ of Eq. (8) and then minimize it with respect to λ_0 we find the equation

$$\frac{d}{d\lambda_0}\left[k\left(\lambda_0^2 - q\right)^2 + 2\lambda_0^2 + \lambda_0^{-4}\right] = 0. \tag{11}$$

The value of λ_0 found by solving (11) can be used to convert deformations to start from the Sm-A state as: follows

$$\mathbf{F} = \mathbf{F}_{\text{Sm-}A} \cdot \mathbf{F}_0. \tag{12}$$

If we substitute this transformation into the free energy then the uniaxial deformation $\mathbf{F}_0$ results in the scaling of b and d by λ_0^{-2} and scaling of the term $|\mathbf{F}\cdot\mathbf{n}_0|^2$ by λ_0^{-4}. We will define the scaled quantities

$$\tilde{b} = b/\lambda_0^2, \tag{13}$$

$$\tilde{d} = d/\lambda_0^2 \tag{14}$$

to describe b and d from the Sm-A reference state. The total free energy with respect to the Sm-A state (denoted with a tilde) is

$$\widetilde{W}^{qc}(\mathbf{F}_{\text{Sm-}A}) = \begin{cases} \lambda_0^{-4}|\mathbf{F}_{\text{Sm-}A}\cdot\mathbf{n}_0|^2 + f\left(\lambda_0^2\tilde{b},\lambda_0^2\tilde{d}\right), & \det\mathbf{F}_{\text{Sm-}A} = 1, \\ \infty & \text{otherwise.} \end{cases} \tag{15}$$

For the rest of this paper we will only refer to deformations with respect to the Sm-A reference state, so we will drop the subscript on $\mathbf{F}_{\text{Sm-}A}$.

The phase diagram of the quasiconvex free energy is illustrated in Fig. 2. Note the region with $\tilde{d} > \tilde{b}$ is inaccessible for volume conserving deformations. In the anisotropic solid (AS) phase the quasiconvex free energy and the microscopic free energy are the same. The energy is not lowered by the formation of microstructure and the smectic layers do not buckle. Hence the small-angle x-ray-scattering pattern should show just one orientation of the layer normal. In the unidirectional buckling (UB) phase the energy is minimized by the formation of a simple laminate [22]. There are two deformation gradients $\mathbf{F}_A$ and $\mathbf{F}_B$ that are rank-one connected and whose suitably weighted average produces the macroscopic deformation. The small-angle x-ray-scattering pattern will contain two orientations of the layer normal corresponding to the regions of $\mathbf{F}_A$ and $\mathbf{F}_B$. There should be no reduction in x-ray-scattering intensity if the x-ray beam is normal to the plane in which the laminate forms. In the bidirectional buckling (BB) phase there is no simple laminate that can achieve the optimal energy. A higher-order laminate must be formed [22]. Here the microstructure contains an average of several different deformation gradients. Physically buckling of the smectic layers in more than one direction is possible and it is expected that the small-angle x-ray-scattering pattern will show a loss of intensity, indicating that some smectic layers are rotated out of the scattering plane.

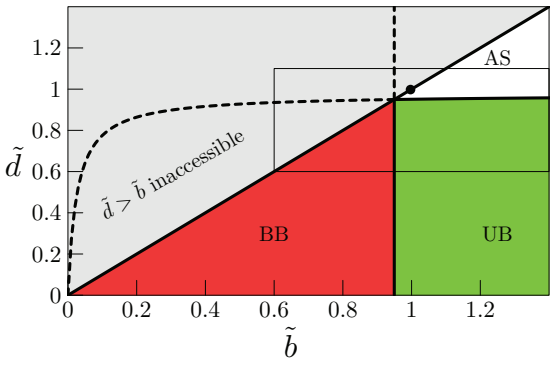

FIG. 2. (Color online) Phase diagram of the Sm-A LCE quasiconvex energy indicating the anisotropic solid (AS), unidirectional buckling (UB), and bidirectional buckling (BB) phases. The phase of the deformation is determined by $\tilde{b}$ and $\tilde{d}$ given in Eqs. (13) and (14). The Sm-A equilibrium point is marked by a black circle.

The three phases could be distinguishable using a crossed polarizer-analyzer pair. The optical axis is parallel to the director. The AS phase will appear dark when the polarizer (or analyzer) is parallel to the optical axis and has maximum brightness when the polarizer is at 45° to the optical axis. In the BB phase the director varies rapidly in both buckling directions, so it will always be bright when viewed between the polarizer and analyzer. In the UB phase the simple laminates associated with the unidirectional layer buckling will be visible as striped domains, much like nematic elastomers. We anticipate that both the BB phase and the UB phase will be optically opaque, just as in the striped domains in nematic elastomers (see Refs. [26,27] and Fig. 8.10 of Ref. [31]).

B. Smectic layer buckling, finite extensibility, and entanglements

The Gaussian phantom chain network model neglects effects such as finite extensibility of the polymer chains and the entanglements of chains with their neighbor. Several theoretical approaches have been pursued to correct for these effects [32,33].

The quasiconvex free energy in Eq. (8) is formulated on the assumption that an infinitely fine microstructure can be formed at no energy cost. Energy terms involving gradients of the deformation, arising through the Frank elastic cost of gradients in the director, will give rise to an interfacial energy cost. Deformations perpendicular to the layer normal will distort the buckled layers changing the interfacial energy.

In the BB phase $\widetilde{W}^{qc}$ is independent of $\tilde{b}$ and $\tilde{d}$, so it does not reproduce the Poisson ratios of $(\frac{1}{2},\frac{1}{2})$ seen in experiment. Motivated by the above theoretical considerations and to recover the experimentally observed Poisson ratios we will include an additional term that physically relates to the non-Gaussian nature of the polymer chains and the deformation of the buckled layers.

We will include in the energy a phenomenological Mooney-Rivlin-type term proportional to the second invariant of the Cauchy-Green strain tensor $\mathbf{C} = \mathbf{F}^T \cdot \mathbf{F}$ [34,35],

$$\widetilde{W}_{MR}(\mathbf{F}) = \tfrac{1}{2} c_{MR}(\mathrm{Tr}[\mathbf{C}]^2 - \mathrm{Tr}[\mathbf{C}\cdot\mathbf{C}]). \tag{16}$$

Note that the Mooney-Rivlin model is overly simplistic in assuming that the derivatives of the energy with respect to the first and second invariants [denoted A_1 and A_2, respectively, in Eqs. (31) and (32)] $\frac{\partial W}{\partial A_1}$ and $\frac{\partial W}{\partial A_2}$ are constants, so it does not realistically describe the uniaxial or biaxial stretching of even isotropic rubbers [32,36,37]. Consequently the values of coefficients fitted to experiments are likely to be only approximate.

The total free energy

$$\widetilde{W}_{\mathrm{tot}} = \widetilde{W}^{qc} + \widetilde{W}_{MR} \tag{17}$$

is altogether polyconvex as both terms are individually polyconvex [38]. It can be shown by constructing a one-dimensional example that the quasiconvex envelope of the sum of two functions is not in general equal to the sum of their quasiconvex envelopes. If we were to add the Mooney-Rivlin term to the nonconvex free energy of Eq. (1) then the quasiconvex envelope of their sum differs from $\widetilde{W}_{\mathrm{tot}}$ in Eq. (17). The small shift in the energy wells will not alter the qualitative features of the numerical results here, so we will neglect this change.

The magnitude of this additional term arising from deforming the buckled layers can be estimated through dimensional analysis as follows. The free energy cost per unit area of interface in the microstructure can be estimated as $\sqrt{KB}$, where K is the Frank elastic constant and B the liquid smectic modulus. The length scale of the microstructure is given by the geometric mean of the sample size parallel to the layer normal L_x and the typical layer dimension, i.e., $\sqrt{L_x\sqrt{\frac{K}{B}}}$. Using dimensional analysis we can form an elastic modulus for the buckled layers by dividing these two quantities

$$B\sqrt{\sqrt{\frac{K}{B}}\frac{1}{L_x}}. \tag{18}$$

Note that the buckled layer modulus goes to zero when $K = 0$ as expected. A more detailed calculation that produces a similar result for the modulus is given in Appendix B. The contribution to c_{MR} from layer buckling in appropriate dimensionless units is

$$c_{MR} \sim \frac{2B}{\mu r^{1/3}}\sqrt{\sqrt{\frac{K}{B}}\frac{1}{L_x}}. \tag{19}$$

Here $\widetilde{W}_{MR}$ has a minimum when $\mathbf{F} = \mathbf{I}$. If we substitute the deformation

$$\mathbf{F} = \begin{pmatrix} 1 & 0 & 0 \\ 0 & \lambda & 0 \\ 0 & 0 & \frac{1}{\lambda} \end{pmatrix} \tag{20}$$

into Eq. (16) it produces

$$\widetilde{W}_{MR}(\mathbf{F}) = 3c_{MR} + 4c_{MR}(\lambda - 1)^2 + O(\lambda - 1)^3. \tag{21}$$

Hence this additional term is minimal when the deformations in the two transverse directions are equal. Consequently it will act to equalize the Poisson ratios, as seen in experiment.

Note that this additional term affects all the phases, not just the BB phase. However, it is not the dominant free energy term in the AS and UB phases, so it does not alter the physics of the model there.

TABLE I. Model parameters.

Parameter (symbol)	Value
B	3.6×10^6 Pa
μ	10^5 Pa
r	1.95
K	10^{-11} N
λ_0	0.895
k	48.4
q	0.780
c_{MR}	0.14

C. Model parameters

Our aim here is to model side-chain Sm-A elastomer samples similar to those of Nishikawa *et al.* [4,5], hence we will use the material parameters listed in Table I for the smectic layer modulus B, the rubber shear modulus μ, and a polymer anisotropy r appropriate for a prolate side-chain LCP. Equations (2), (3), and (11) can then be used to find q, k, and λ_0.

We will use a value of the Mooney-Rivlin coefficient $c_{MR} = 0.14$ in finite element calculations. This can be estimated from Eq. (19) with $L_x \sim 1$ cm. Determination of this value is discussed in Sec. IV. However, it is consistent with the work of Stannarius *et al.*, who performed mechanical experiments on Sm-A LCE balloons and found Mooney-Rivlin coefficients in the range $0 < c_{MR} < 0.1$ [11].

III. UNIFORM DEFORMATIONS

To develop an intuition for the quasiconvex free energy in Eq. (15) we will now examine some uniform deformations. Here we will assume that the layer normal is aligned with the **x** direction, i.e., $\mathbf{n}_0 = (1,0,0)^T$.

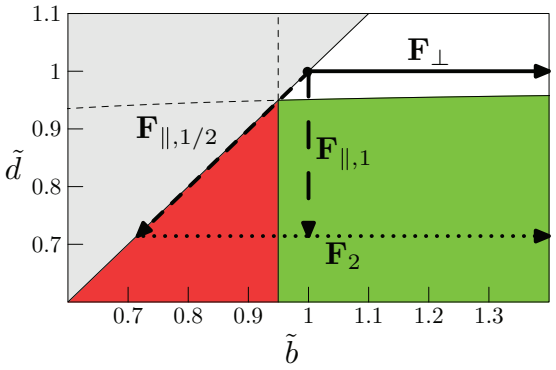

FIG. 3. (Color online) Paths traversed in $\tilde{b}$ and $\tilde{d}$ on stretching parallel to $\mathbf{n}_0$ with (short-dashed line) $\gamma = \frac{1}{2}$ and (long-dashed line) $\gamma = 1$. The solid line and the dotted line are stretches perpendicular to $\mathbf{n}_0$, with the latter performed after an initial parallel to $\mathbf{n}_0$.

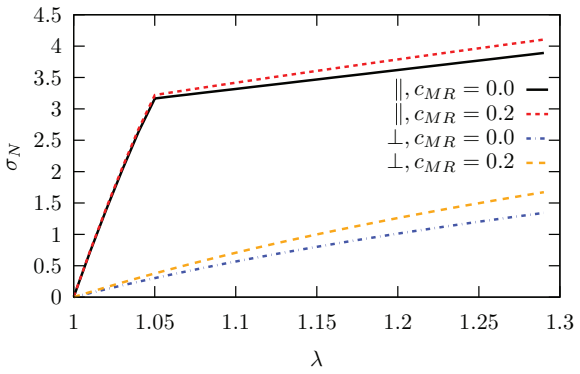

FIG. 4. (Color online) Nominal stress σ_N as a function of deformation λ parallel to $\mathbf{n}_0$ with $\gamma = \frac{1}{2}$ and perpendicular to $\mathbf{n}_0$.

A. Elongation parallel to the layer normal

An elongation parallel to the layer normal is described by

$$\mathbf{F}_\parallel = \begin{pmatrix} \lambda & 0 & 0 \\ 0 & \frac{1}{\lambda^\gamma} & 0 \\ 0 & 0 & \frac{1}{\lambda^{1-\gamma}} \end{pmatrix}, \tag{22}$$

where the parameter γ determines the Poisson ratio of the deformation. A value of $\gamma = \frac{1}{2}$ gives isotropic behavior in the directions perpendicular to $\mathbf{n}_0$. A value of $\gamma = 1$ gives the anisotropic Poisson ratios of (1,0). Figure 3 shows the boxed area of the phase diagram in Fig. 2 and illustrates that when stretching parallel to $\mathbf{n}_0$ with $\gamma = \frac{1}{2}$ (labeled $\mathbf{F}_{\parallel,1/2}$ in Fig. 3) the elastomer deformation follows the line $\tilde{b} = \tilde{d}$. The system crosses from the AS to BB phase at a threshold deformation $\lambda_{\rm th} = \lambda_0^2(q - 1/k)^{-1}$. By contrast, when stretching parallel to $\mathbf{n}_0$ with $\gamma = 1$ the elastomer deformation follows the line of constant $\tilde{b}$ (labeled $\mathbf{F}_{\parallel,1}$ in Fig. 3).

The nominal stress denoted σ_N and measured in units of $\frac{1}{2}\mu r^{1/3}$ can be calculated by differentiating the scaled free energy $\widetilde{W}_{\rm tot}$ with respect to λ. The nominal stress shows a dramatic reduction when the elastomer crosses into the microstructured phases BB or UB. For example, on the $\gamma = \frac{1}{2}$ trajectory the elastic modulus when the deformation begins is

$$k\frac{\lambda_0^4}{\lambda_{\rm th}} + \frac{4}{\lambda_0^4} + 6c_{MR}. \tag{23}$$

This is dominated by the smectic layer modulus encoded in $k \gg 1$. After the threshold at $\lambda_{\rm th}$ the modulus drops to

$$\frac{2}{\lambda_0^4} + \frac{6}{\lambda_{\rm th}^4}c_{MR}, \tag{24}$$

i.e., it is reduced by a factor of approximately k. This reduction in the modulus is illustrated in Fig. 4.

B. Elongation perpendicular to the layer normal

An elongation perpendicular to the layer normal $\mathbf{n}_0$, with Poisson ratios of (1,0), is described by

$$\mathbf{F}_\perp = \begin{pmatrix} 1 & 0 & 0 \\ 0 & \lambda & 0 \\ 0 & 0 & \frac{1}{\lambda} \end{pmatrix}. \tag{25}$$

The trajectory of this deformation is along a line of constant $\tilde{d}$, as shown in Fig. 3 (labeled $\mathbf{F}_\perp$). The elastic modulus in this case is

$$8\lambda_0^2 + 8c_{MR}. \tag{26}$$

The nominal stress σ_N for this geometry is illustrated in Fig. 4. There is no threshold in this stress-strain curve and no microstructure forms in this deformation geometry.

C. Two-step deformation

A two-stage deformation process first parallel to the layer normal by a factor of λ_1 and then perpendicular to it by a factor λ_2, defined in Eq. (27), can be used to experimentally determine the constant c_{MR},

$$\mathbf{F}_2 = \begin{pmatrix} 1 & 0 & 0 \\ 0 & \lambda_2 & 0 \\ 0 & 0 & \frac{1}{\lambda_2} \end{pmatrix} \cdot \begin{pmatrix} \lambda_1 & 0 & 0 \\ 0 & \frac{1}{\sqrt{\lambda_1}} & 0 \\ 0 & 0 & \frac{1}{\sqrt{\lambda_1}} \end{pmatrix}. \tag{27}$$

The trajectory of this deformation is illustrated in Fig. 3. The first stage follows $\mathbf{F}_{\parallel,1/2}$ and the second stage is labeled $\mathbf{F}_2$. The first stage of deformation proceeds as the system moves along the line $\tilde{b} = \tilde{d}$, thus crossing from the AS to the BB phase. During the second deformation stage the system moves along a line of constant $\tilde{d}$, crossing from the BB to the UB phase. The nominal stress during the second stage is shown in Fig. 5. If c_{MR} is zero then the deformation is perfectly soft within the BB phase. This is an intrinsic property of $\widetilde{W}^{qc}(\mathbf{F})$, which is altered by the addition of $\widetilde{W}_{MR}$. Physically this reflects the fact that there is an energetic cost to deforming buckled layers, which rules out perfectly soft deformation. At the start of the λ_2 deformation the elastic modulus is given by

$$8c_{MR}\lambda_1, \tag{28}$$

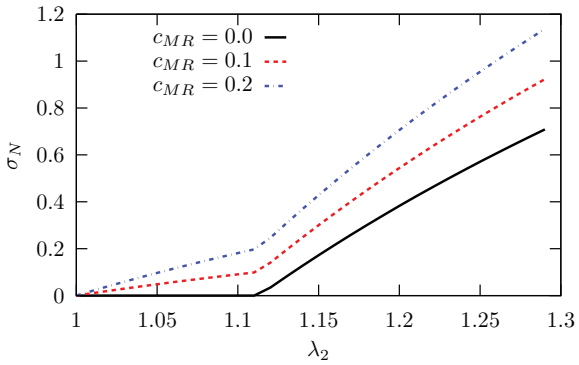

FIG. 5. (Color online) Nominal stress as a function of deformation λ_2 during the two-stage deformation. The first stage is a deformation parallel to $\mathbf{n}_0$ of $\lambda_1 = 1.4$, followed by the perpendicular elongation λ_2.

i.e., it is entirely due to the additional Mooney-Rivlin term, so can be used to experimentally measure this additional constant. Once the trajectory of the deformation enters the UB phase the stiffness increases to

$$8q + 8/(qk^2) - 16/k + 8c_{MR}\lambda_1. \tag{29}$$

D. Elongation at an angle to the layer normal

Elongation of the elastomer at an angle θ to the layer normal can be represented by the deformation

$$\mathbf{F} = \begin{pmatrix} \lambda & 0 & 0 \\ 0 & \frac{1}{\sqrt{\lambda}} & 0 \\ 0 & 0 & \frac{1}{\sqrt{\lambda}} \end{pmatrix} \cdot \begin{pmatrix} \cos\theta & \sin\theta & 0 \\ -\sin\theta & \cos\theta & 0 \\ 0 & 0 & 1 \end{pmatrix}. \tag{30}$$

Two trajectories for this type of deformation are shown on the phase diagram in Fig. 6 for $\theta = 17^\circ$ and 23°. Elongation at an angle to the layer normal results in a rapid rotation of the layer normal away from the stretch axis. The lowest free energy of the system for larger rotation angles is in the UB phase, as illustrated by the trajectory of the deformation.

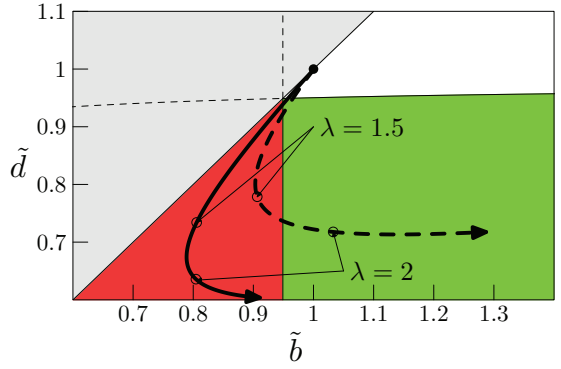

FIG. 6. (Color online) Trajectories on the phase diagram for elongations at an angle of $\theta = 17^\circ$ (solid line) and $\theta = 23^\circ$ (dashed line) to $\mathbf{n}_0$. The maximum deformation shown in each case corresponds to $\lambda = 2.5$.

IV. FINITE ELEMENT MODEL

A. Method

The free energy in Eq. (17) derived from Eqs. (15) and (16) has one direction of anisotropy $\mathbf{n}_0$. It can be written using the following invariants of the Cauchy-Green strain tensor $\mathbf{C} = \mathbf{F}^T \cdot \mathbf{F}$:

$$A_1 = \mathrm{Tr}[\mathbf{C}], \tag{31}$$

$$A_2 = \tfrac{1}{2}(\mathrm{Tr}[\mathbf{C}]^2 - \mathrm{Tr}[\mathbf{C}\cdot\mathbf{C}]), \tag{32}$$

$$A_3 = \det[\mathbf{C}], \tag{33}$$

$$A_4 = \mathbf{n}_0 \cdot \mathbf{C} \cdot \mathbf{n}_0, \tag{34}$$

$$A_5 = \mathbf{n}_0 \cdot \mathbf{C} \cdot \mathbf{C} \cdot \mathbf{n}_0. \tag{35}$$

The parameters $\tilde{b}$ and $\tilde{d}$ can be rewritten as

$$\tilde{b} = \frac{A_1 - A_4 + \sqrt{(A_1 + A_4)^2 - 4(A_2 + A_5)}}{2}, \tag{36}$$

$$\tilde{d} = \sqrt{A_2 + A_5 - A_1 A_4}. \tag{37}$$

The Mooney-Rivlin term can be rewritten as

$$W_{MR}(\mathbf{F}) = c_{MR} A_2. \tag{38}$$

Some care must be taken in treating these expressions numerically. First, in Eq. (36) the two terms $(A_1 + A_4)^2$ and $4(A_2 + A_5)$ are typically close together. This subtractive cancellation can lead to large numerical errors. Second, we require the derivatives of the free energy to compute the stresses in the material. Differentiating the square root expression in Eq. (36) gives an expression that diverges when $(A_1 + A_4)^2 = 4(A_2 + A_5)$. It is useful to smooth the divergence in this expression by adding a small value $\epsilon \sim 10^{-5}$ to the contents of the square root.

The material energy $\tilde{W}_{\mathrm{tot}}(\mathbf{F})$ was implemented in the commercial finite element package `Abaqus 6.10` [39] by writing a `UANISOHYPER_INV` subroutine for the standard implicit integration scheme. The numerical method in this routine is based on previous work implementing invariant based elasticity [40,41]. Incompressibility is enforced within this code by specifying `type=incompressible` in the material definition. The anisotropy parameter `local directions=1` is specified, with the local direction defined as $\mathbf{n}_0$.

Rigid clamping boundary conditions were used on the end faces of the elastomer. In `Abaqus` these constraints are implemented as pinned displacement boundary conditions, e.g., `U1=0.64`, `U2=0`, and `U3=0` at the mobile clamp. Experimentally an alternative to rigid clamping is to secure the ends of the elastomer with tape, which allows a contraction in thickness of the elastomer at the clamp. Simulations using tapelike boundary conditions produce very similar stress-strain curves to rigid clamping with a slight difference in microstructure near the clamps.

The elastomer was deformed by moving one of the clamps to achieve a total deformation of $\lambda = 1.4$. The step size increment was fixed at 5×10^{-3}.

B. Mesh verification

Initial tests of the UANISOHYPER_INV subroutine were conducted on a single C3D8H (eight-node linear brick hybrid) element. These showed that the model is correctly equilibrated, as no stresses were present at zero deformation. When stretching parallel to $\mathbf{n}_0$ the expected stress-strain curve was reproduced. Integration points undergo a transition from the AS to BB phase at the correct threshold strain. The subroutine was then tested with C3D8RH (reduced-integration) and C3D20H (20-node) elements and it was confirmed that the results were independent of the element type.

The thin film was represented using uniform meshes with between 800 ($40 \times 20 \times 1$) and 32 000 ($200 \times 160 \times 1$) elements. These meshes were observed to achieve equivalent results. Computations were also performed using biased meshes, which achieved stress solutions within 0.5% of uniform meshes. Equivalent results were also obtained with thicker meshes ($100 \times 50 \times 5$). The results presented in the following sections were obtained using a rectangular uniform mesh of 5000 ($100 \times 50 \times 1$) C3D8H elements.

C. Parameters

Motivated by the work of Nishikawa and Finkelmann [5], we will start by investigating a sample consisting of a rectangular cuboid of dimensions 1.6 cm × 1.0 cm × 500 μm. The value of the layer buckling term c_{MR} can be estimated by examining its effect on the fractional change of the width of the sample W/W_0 when stretching parallel to $\mathbf{n}_0$. The width of the middle of the sample was measured as a function of deformation. Figure 7 shows that if $c_{MR} = 0$ the width of the sample remains constant above the threshold. A value of $c_{MR} = 0.14$ successfully approximates the deformed state seen in Fig. 4. of Ref. [5]. The other parameters used in the finite element calculations are as presented in Table I.

V. RESULTS AND DISCUSSION

A. Elongation parallel and perpendicular to the layer normal

The stress-strain curve for deformation parallel to $\mathbf{n}_0$ is shown in Fig. 8. This curve, obtained from finite element modeling, is in agreement with the stress-strain curve obtained

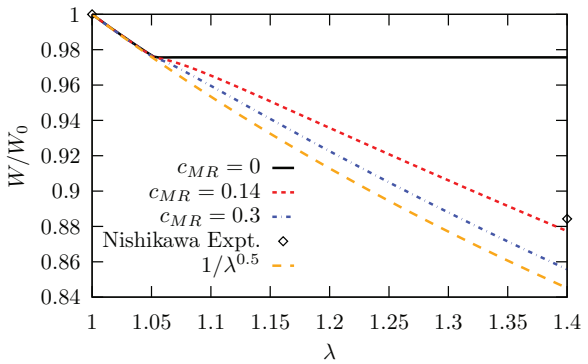

FIG. 7. (Color online) Deformation across the width of the sample in the target state as a function of the deformation applied parallel to $\mathbf{n}_0$.

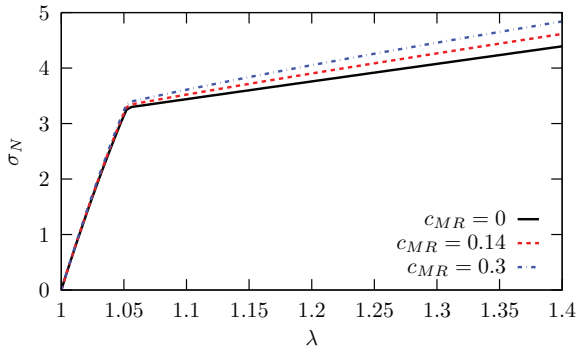

FIG. 8. (Color online) Nominal stress as a function of deformation parallel to $\mathbf{n}_0$ for different values of c_{MR}.

for a uniform deformation shown in Fig. 4. The spatial distribution of phase of the sample is shown in Fig. 9(a). The bulk of the sample is in the BB phase, however, the UB phase is present in the vicinity of the clamps. Near the clamps the elastomer is constrained in a way that prevents isotropic deformation, meaning they tend to form a UB microstructure rather than a BB microstructure. The shape of the deformed sample is similar to that of the isotropic neo-Hookean elastomer shown in Fig. 9(c). Note that for larger values of B/μ the threshold for the transition to the buckled layer state happens at a lower value of strain and the UB regions near the clamps are smaller.

On deforming the sample perpendicular to $\mathbf{n}_0$ no buckled microstructure forms, as shown Fig. 9(b). This behavior is consistent with the uniform deformation case shown in Fig. 3. The layer spacing is constant and the sample deforms with Poisson ratios of (1,0).

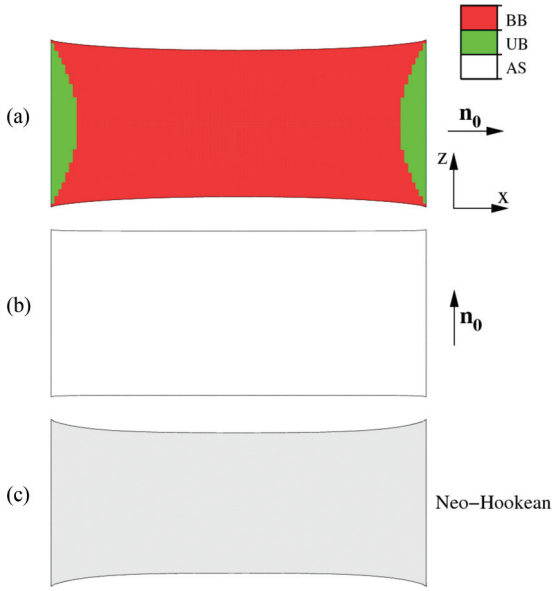

FIG. 9. (Color online) Microstructure distribution when stretched in the **x** direction (a) parallel to $\mathbf{n}_0$ and (b) perpendicular to $\mathbf{n}_0$, shown at a deformation of 1.4. (c) Isotropic neo-Hookean sample, with free energy $W(\mathbf{F}) = C_1(A_1 - 3) + \frac{1}{D_1}(A_3 - 1)^2$, where $C_1 = 2$ and $D_1 = 10^{-6}$.

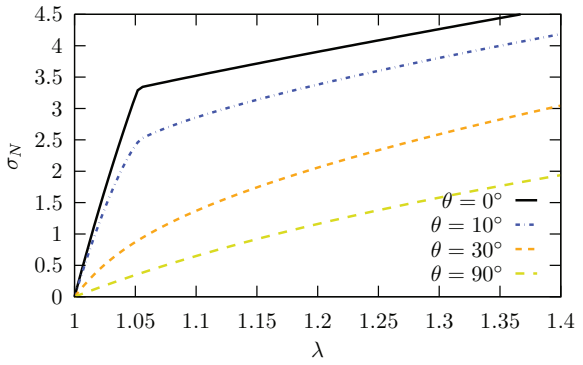

FIG. 10. (Color online) Nominal stress as a function of deformation, where $\mathbf{n}_0$ is oriented in the plane of the film at an angle θ to the elongation axis.

B. Elongation at an arbitrary angle to the layer normal

The stress-strain behavior for elongations at various angles to $\mathbf{n}_0$ are shown in Fig. 10 for an elastomer with the same aspect ratio as those of Nishikawa *et al*. For elongations within $\sim 10^\circ$ of $\mathbf{n}_0$ the stress-strain curve still resembles that of the parallel case. However, for elongations at $\sim 20^\circ$ and above there is no longer a well defined threshold transition to a lower modulus. The corresponding spatial distribution of the microstructure for elongations at various angles to $\mathbf{n}_0$ is shown in Fig. 11. These results show that elongations at an angle within $\sim 1^\circ$ of the $\mathbf{n}_0$ result in the BB phase forming in the bulk of the sample, with a UB phase at the clamps. Note that for angles above $\sim 20^\circ$ there is no percolation of the strip of the UB or BB phase across the sample. This coincides with the disappearance of the threshold in the stress-strain response. At a stretching angle of 2° the UB phase forms at the free edges of the sample. The formation of the UB microstructure is accompanied by λ_{xz} shears present in these regions of the sample.

We will now examine the deformation of the sample with a 5° inclination of the layer normal in more depth. The phase distribution and the shear deformation are shown in Figs. 12(a) and 12(b), respectively. The deformation of the mesh shows the shear deformation of the elements. Only the weakly sheared central area of the sample is in the BB phase. Strong shears result in a transition from the BB to the UB phase. The transition occurs at $\lambda_{xz} \sim 0.4$ for an imposed deformation of $\lambda_{xx} = 1.4$ or, equivalently, an engineering shear strain of $\gamma_{xz} = (\lambda_{xz} + \lambda_{zx})/2 \sim 0.2$.

We can understand these results and the transformation of the sample phase by considering a deformation at an angle θ to $\mathbf{n}_0$ consisting of an elongation λ_1 and a shear λ_{xz},

$$\mathbf{F} = \begin{pmatrix} \lambda_1 & 0 & \lambda_{xz} \\ 0 & \frac{1}{\lambda_1^\gamma} & 0 \\ 0 & 0 & \frac{1}{\lambda_1^{\gamma-1}} \end{pmatrix} \cdot \begin{pmatrix} \cos\theta & \sin\theta & 0 \\ -\sin\theta & \cos\theta & 0 \\ 0 & 0 & 1 \end{pmatrix}. \quad (39)$$

The state of the elements from the slice across the sample in Fig. 12(a) in the $(\tilde{b},\tilde{d})$ phase space is shown in Fig. 13. As we cross the center of the sample, the elements are in the BB phase. The elements are subjected to an increased amount of shear,

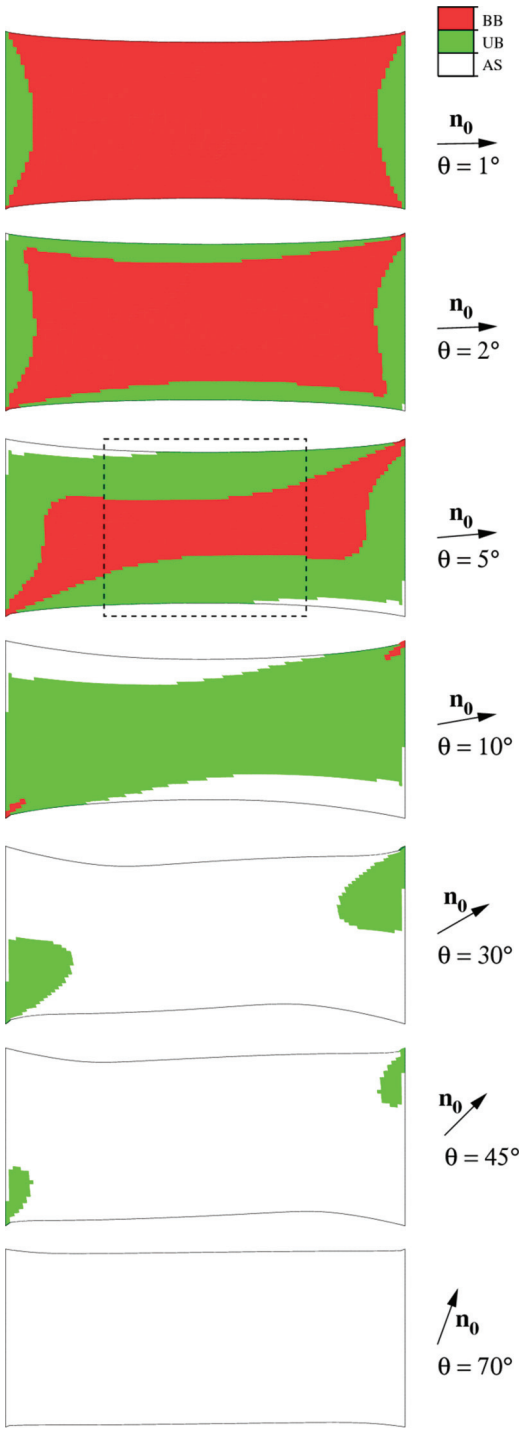

FIG. 11. (Color online) Microstructure distribution for elongation at 1°, 2°, 5°, 10°, 45°, and 70° to $\mathbf{n}_0$, shown at a deformation of $\lambda = 1.4$. The dashed region is explored in more detailed in Fig. 12.

which is illustrated by the trajectory labeled $\mathbf{F}_1$ in Fig. 13. Once the edge of the BB phase is reached the thickness of the sample increases, and the sample transitions to the UB phase. As the UB phase consists of buckling in only one direction, it is thicker in the direction perpendicular to the plane in which the microstructure laminates are formed. This is illustrated by the trajectory $\mathbf{F}_2$ in Fig. 13.

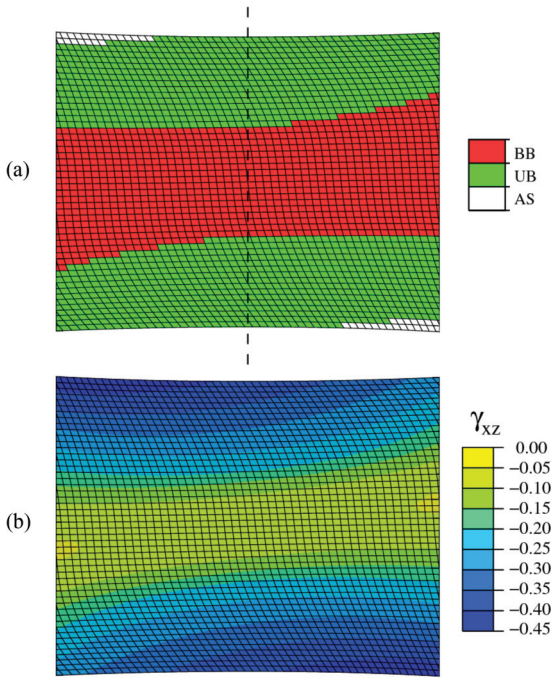

FIG. 12. (Color online) (a) Spatial microstructure distribution and (b) γ_{xz} engineering shear strain, for the dashed region of Fig. 11.

C. Aspect ratio

So far we have only considered samples with the same aspect ratio as those studied by Nishikawa and Finkelmann [5]. Other work on Sm-*A* elastomers has used very different sample aspect ratios, such as those used by Komp and Finkelmann [7] (2 cm × 4 mm × 100 μm). The finite element results shown in Fig. 14 show that varying the length-to-width ratio of the sample at constant film thickness alters the stress-strain curves obtained when at a small angle to $\mathbf{n}_0$, but produce the same stress-strain curves when stretching exactly parallel to $\mathbf{n}_0$.

The spatial microstructure distribution is highly sensitive to the aspect ratio. Figure 15 shows the microstructure distribution in a sample with an aspect ratio of 8. When compared to Fig. 11, where the aspect ratio is 1.6, it can

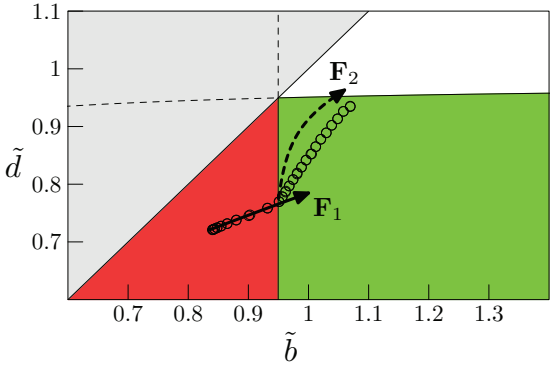

FIG. 13. (Color online) Phase of the elements across the sample in Fig. 12(a) in the $(\tilde{b},\tilde{d})$ phase space (open circles). The trajectory $\mathbf{F}_1$ is a deformation with $\gamma = 0.73$, $\theta = 5^\circ$, $\lambda_1 = 1.4$, and $\lambda_{xz} = 0$ to 0.4 (solid line). The trajectory $\mathbf{F}_2$ is a deformation with $\gamma = 0.1$, $\theta = 5^\circ$, $\lambda_1 = 1.4$, and $\lambda_{xz} = 0.4$ to 0.7 (dashed line).

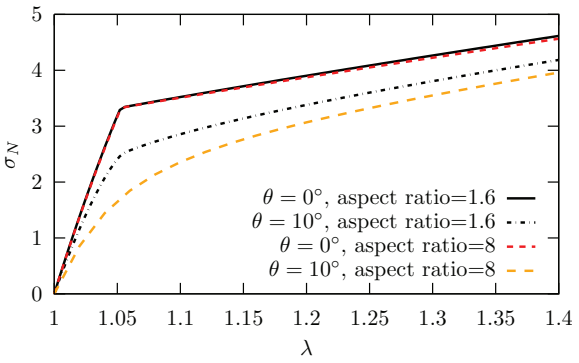

FIG. 14. (Color online) Nominal stress as a function of deformation for elongation at 0° and 10° to $\mathbf{n}_0$ for aspect ratios of 1.6 and 8.

be seen that the larger aspect ratio reverts to the AS phase for smaller angles of inclination of the deformation to the layer normal. Qualitatively this is because a smaller fraction of the sample is taken up by the end region near the clamps as the aspect ratio increases. Hence the layer normal is less constrained in its rotation by these end regions and can adopt the lowest energy orientation rotated away from the elongation axis. For the aspect ratio of 8 an inclination as little as 2° results in the sample forming the UB phase rather than the BB phase. This may make it difficult to experimentally observe the BB microstructure in high aspect ratio samples by stretching parallel to $\mathbf{n}_0$. The sensitivity of the microstructure to the deformation direction is increased for larger values of B/μ.

The effects of aspect ratio are summarized in Fig. 16, which shows the phase present in the center of the sample for various aspect ratios and stretching angles. The lowest aspect ratio forms the UB phase for all stretching angles 0°–10°, as the effect of the clamps dominates the whole sample. For higher aspect ratios the effect of the clamps on the center of the

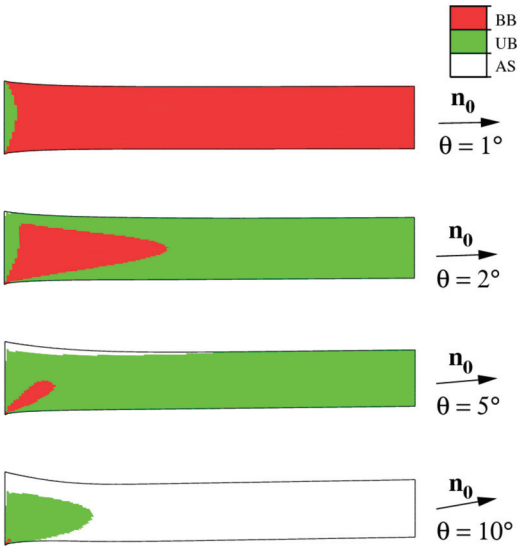

FIG. 15. (Color online) Microstructure distribution when stretching at 1°, 2°, 5°, and 10° to $\mathbf{n}_0$ at a strain of 0.4. The sample dimensions are 8.0 cm × 1.0 cm × 500 μm, which is an aspect ratio of 8. Only half of the samples are depicted here.

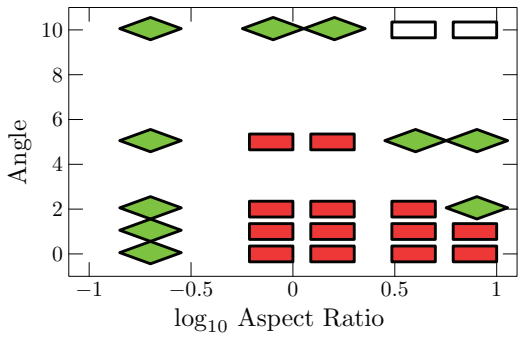

FIG. 16. (Color online) Phase found in the center of the sample at a deformation of $\lambda = 1.4$ for various aspect ratios and stretching angles relative to $\mathbf{n}_0$.

sample diminishes and the BB phase forms for very small angles. However, a small deviation from stretching parallel to the layer normal results in a reversion back to the UB phase. Experimental studies on higher aspect ratio samples [7] show no opacity after the stress-strain threshold. It is tempting to associate this with a small misalignment of the stretch axis with the layer normal, resulting in the UB or (for large angles) the AS phase. However, the small-angle x-ray scattering does not support this as there is no reorientation of the layer normal observed in this experiment. Varying the thickness of the sample at a constant length-to-width ratio results in qualitatively similar stress-strain curves and microstructure distribution.

VI. CONCLUSION

We have simulated the stretching of monodomain Sm-*A* elastomer sheets by using a quasiconvex free energy model [22]. This model was augmented with an energy term to describe the energy of deforming buckled layers, which is necessary to reproduce the experimentally observed Poisson ratios. The magnitude of this term can be measured experimentally by a two-step deformation process: first deforming the elastomer parallel to the layer normal and then deforming perpendicular to this direction. The modulus of the elastomer during this second step gives the modulus of the additional energy term.

The deformation of the elastomer in realistic experimental geometries was computed using finite elements. The tensile deformation of Sm-*A* elastomer sheets of different aspect ratios and with different angles between the stretch axis and the layer normal was investigated. When elongated parallel to $\mathbf{n}_0$ the majority of the sample is predicted to form a bidirectionally buckled microstructure, except at the clamps, where a unidirectional microstructure is expected.

Experimentally the microstructural differences should be distinguishable using x-ray-scattering patterns or by examination through a polarizer-analyzer pair as described at the end of Sec. II A. When elongated at a small inclination to the layer normal the phase of the sample is sensitive to the aspect ratio of the sample. For low aspect ratios the bidirectionally buckled phase persists to large angles. For high aspect ratios no buckled phase is observed in the bulk of the sample even for small inclination angles of a few degrees between the stretch axis and the layer normal.

ACKNOWLEDGMENTS

We would like to thank SEPnet for supporting this project and Dr. Daniel Corbett and Dr. Jon Bevan for helpful discussions.

APPENDIX A: CHANGE OF REFERENCE STATE OF THE SMECTIC-*A* MODEL

We start from the free energy density derived in Ref. [18], given by

$$f_{\text{Sm-}A} = \frac{1}{2}\mu \,\mathrm{Tr}[\boldsymbol{\lambda}\cdot\boldsymbol{\ell}_0\cdot\boldsymbol{\lambda}^T\cdot\boldsymbol{\ell}^{-1}] + \frac{1}{2}B\left(\frac{d}{d_0}-1\right)^2, \tag{A1}$$

where μ is the shear modulus and $\boldsymbol{\lambda}$ is the deformation gradient starting from the smectic reference state with $\det\boldsymbol{\lambda}=1$, as is convention in Ref. [31]. The initial polymer conformation with anisotropy of r and mesogen alignment along the unit vector $\mathbf{n}_0$ is represented by $\boldsymbol{\ell}_0 = \mathbf{I} + (r-1)\mathbf{n}_0\mathbf{n}_0^T$. In the target state the mesogens align parallel to $\mathbf{n}$ and hence the polymer conformation is described by $\boldsymbol{\ell}^{-1} = \mathbf{I} + (\frac{1}{r}-1)\mathbf{n}\mathbf{n}^T$. Additionally B is the smectic layer modulus, d is the current layer spacing, and d_0 is the equilibrium layer spacing. The layer normal orientation denoted by the unit vector $\mathbf{n}$ is assumed to deform like an embedded plane, hence

$$\mathbf{n} = \frac{\mathrm{cof}\,\boldsymbol{\lambda}\cdot\mathbf{n}_0}{|\mathrm{cof}\,\boldsymbol{\lambda}\cdot\mathbf{n}_0|}, \tag{A2}$$

$$\frac{d}{d_0} = \frac{1}{|\mathrm{cof}\,\boldsymbol{\lambda}\cdot\mathbf{n}_0|}, \tag{A3}$$

where $\mathbf{n}$ is the current layer normal, $\mathbf{n}_0$ is the initial layer normal, and $\mathrm{cof}\,\boldsymbol{\lambda} = \boldsymbol{\lambda}^{-T}$ denotes the cofactor of $\boldsymbol{\lambda}$ for volume conserving deformations.

The free energy density in Eq. (A1) can be reexpressed using the high-temperature isotropic state as the reference configuration. The deformations relative to this reference state are given by $\mathbf{F}$, where

$$\mathbf{F} = \boldsymbol{\lambda}\cdot\boldsymbol{\ell}_0^{1/2} r^{-1/6}. \tag{A4}$$

Physically we are first taking the isotropic sample in the reference state and then cooling it to the smectic state, whereupon it undergoes a volume conserving spontaneous deformation $\boldsymbol{\ell}_0^{1/2} r^{-1/6}$. The deformation $\boldsymbol{\lambda}$ is then carried out from the smectic state. The free energy density expressed in terms of $\mathbf{F}$ is

$$f_{\text{Sm-}A} = \frac{1}{2}\mu r^{1/3}\left[\mathrm{Tr}\,\mathbf{F}\cdot\mathbf{F}^T + kq^2\left(\frac{q}{|\mathrm{cof}\,\mathbf{F}\cdot\mathbf{n}_0|}-1\right)^2\right]. \tag{A5}$$

If we assume that $k \gg 1$, then we can make the approximation $|\mathrm{cof}\,\mathbf{F}\cdot\mathbf{n}_0| \approx q$. This expression, when converted to a dimensionless quantity by dividing by $\frac{1}{2}\mu r^{1/3}$, can then be approximated by Eq. (1).

APPENDIX B: ESTIMATION OF THE COEFFICIENT OF THE NEW TERM

The stiffness associated with changing the buckling wavelength of the layers can be estimated by using a calculation similar to that of Finkelmann *et al.* [26]. We first calculate the free energy of a single interface between two regions of opposite shear. Consider a Sm-*A* film with $\mathbf{n}_0 = (1,0,0)^T$. The deformation gradient tensor in the two regions is given by

$$\boldsymbol{\lambda} = \begin{pmatrix} \lambda_{xx} & 0 & \lambda_{xz} \\ 0 & \frac{1}{\lambda_{xx}\lambda_{zz}} & 0 \\ 0 & 0 & \lambda_{zz} \end{pmatrix}. \tag{B1}$$

Using Eqs. (A2) and (A3) this deformation results in the following expression for the layer spacing and director orientation:

$$\frac{d}{d_0} = \frac{\lambda_{xx}\lambda_{zz}}{\sqrt{\lambda_{xx}^2 + \lambda_{xz}^2}}, \tag{B2}$$

$$\mathbf{n} = \left(\frac{\lambda_{zz}}{\sqrt{\lambda_{xx}^2 + \lambda_{xz}^2}}, 0, -\frac{\lambda_{xz}}{\sqrt{\lambda_{xx}^2 + \lambda_{xz}^2}}\right). \tag{B3}$$

The orientation of the layer normal can be written as $\mathbf{n} = (\cos\theta, 0, \sin\theta)$, where $\tan\theta = -\lambda_{xz}/\lambda_{zz}$. If we substitute these expressions into the Sm-*A* free energy expression in Eq. (A1) we obtain

$$f = \frac{1}{2}\mu\left[\lambda_{zz}^2 + \frac{1}{\lambda_{zz}^2\lambda_{xx}^2} + \lambda_{zz}^2\tan^2\theta + (\cos^2\theta + r\sin^2\theta)\lambda_{xx}^2 + \frac{B}{\mu}(\lambda_{xx}\cos\theta - 1)^2\right]. \tag{B4}$$

This equation can be minimized over λ_{zz}^2, resulting in $\lambda_{zz}^2 = \cos\theta/\lambda_{xx}$. Substituting this back into the free energy reduces it to

$$f = \frac{1}{2}\mu\left[\frac{2}{\lambda_{xx}\cos\theta} + \lambda_{xx}^2(\cos^2\theta + r\sin^2\theta) + \frac{B}{\mu}(\lambda_{xx}\cos\theta - 1)^2\right]. \tag{B5}$$

Expanding for small θ up to quartic order, corresponding to small rotations of the layer normal, produces the expression

$$f = \frac{1}{2}\mu\left[p_0 - p_2\theta^2 + \frac{1}{3}p_4\theta^4\right], \tag{B6}$$

$$p_0 = \frac{2}{\lambda_{xx}} + \lambda_{xx}^2 + \frac{B}{\mu}(\lambda_{xx} - 1)^2, \tag{B7}$$

$$p_2 = -\frac{1}{\lambda_{xx}} + \lambda_{xx}^2(r-1) + \frac{B}{\mu}\left(\lambda_{xx}^2 - \lambda_{xx}\right), \tag{B8}$$

$$p_4 = \frac{1}{4}\frac{B}{\mu}\lambda_{xx}(4\lambda_{xx} - 1) + \frac{5}{4\lambda_{xx}} + (1-r)\lambda_{xx}^2. \tag{B9}$$

In addition to the rubber elastic energy, calculation of the interface energy requires a Frank elastic energy. For simplicity, here we use the one constant approximation, hence the total energy is

$$F = L_xL_y\int_0^{L_z} dz\left(\frac{1}{2}\mu\left[p_0 - p_2\theta^2 + \frac{1}{3}p_4\theta^4\right] + \frac{1}{2}K\theta'^2\right), \tag{B10}$$

where the sample dimensions in the x, y, and z directions are denoted by L_x, L_y, and L_z, respectively. It is convenient to convert distance to a dimensionless quantity using $\xi = \sqrt{\frac{K}{\mu}}$. If we define $t = z/\xi$, then the free energy becomes

$$F = \frac{1}{2}\mu L_xL_y\sqrt{\frac{K}{\mu}}\int_0^{\mathcal{L}} dt\left(\left[p_0 - p_2\theta^2 + \frac{1}{3}p_4\theta^4\right] + \frac{1}{2}\dot{\theta}^2\right), \tag{B11}$$

where $L_z = \mathcal{L}\xi$. Minimization of this integral produces the Euler-Lagrange equation

$$\ddot{\theta} = -p_2\theta + \tfrac{2}{3}p_4\theta^3. \tag{B12}$$

Far away from the interface the director is in the energy minimum where

$$\theta^2 = \theta_0^2 = \frac{3p_2}{2p_4}. \tag{B13}$$

The first integral of the Euler-Lagrange equation is given by

$$\tfrac{1}{2}\dot{\theta}^2 = -\tfrac{1}{2}p_2\theta^2 + \tfrac{1}{6}p_4\theta^4 + \tfrac{1}{2}p_2\theta_0^2 - \tfrac{1}{6}p_4\theta_0^4. \tag{B14}$$

The first integral can be used to substitute for the $\dot{\theta}$ term in the free energy. If we subtract from F the free energy of the uniform state with $\theta = \theta_0$ then we obtain the free energy of the interface

$$F_{\text{int}} = L_xL_y\sqrt{K\mu}\int_0^{\mathcal{L}} dt\left[-p_2\left(\theta^2 - \theta_0^2\right) + \frac{1}{3}p_4\left(\theta^4 - \theta_0^4\right)\right] = \sqrt{2K\mu}\,\frac{p_2^{3/2}}{p_4}L_xL_y. \tag{B15}$$

The wavelength of the layer buckling and hence the stiffness of the buckled layers can be estimated as follows. We assume that the sample can be divided into three regions as shown in Fig. 17. The end regions near the clamps are too constrained to buckle and so contain layers with a fixed layer normal ($\theta = 0$) and hence have free energy density

$$f_U = f_{\theta=0} = \tfrac{1}{2}\mu p_0(\lambda_1), \tag{B16}$$

where λ_1 is the xx component of the deformation in this region. The central region contains smectic layers with tilt angle θ_0

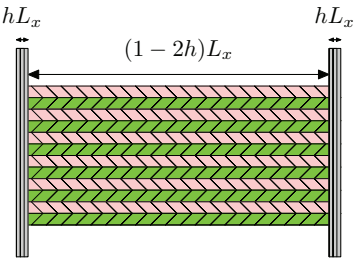

FIG. 17. (Color online) To estimate the length scale of the layer buckling it is assumed that the sample divides into three regions as shown. The end regions do not contain buckled layers, whereas the central region does.

and so has free energy

$$f_R = f_{\theta=\theta_0} = \frac{1}{2}\mu\left(p_0(\lambda_2) - \frac{3}{8}\frac{p_2(\lambda_2)^2}{p_4(\lambda_2)}\right), \tag{B17}$$

where λ_2 is the xx component of the deformation in this region. If the end regions are of order hL_x, which in turn is comparable to the wavelength of the layer buckling, then the number of interfaces in the bulk is $\frac{L_z}{hL_x}$. Since the elongation of the sample is performed by imposing a stress σ, which does work in extending the sample, the total free energy of the system is

$$\begin{aligned} F_T = {} & \frac{1}{2}(1-2h)\mu\left(p_0(\lambda_2) - \frac{3}{8}\frac{p_2(\lambda_2)^2}{p_4(\lambda_2)}\right)V \\ & + h\mu p_0(\lambda_1)V - \sigma(2h\lambda_1 + (1-2h)\lambda_2)V \\ & + F_{\text{int}}\frac{L_z}{hL_x}, \end{aligned} \tag{B18}$$

where $V = L_x L_y L_z$ denotes the volume of the sample. If we minimize this expression over h, then we find the optimal value

$$\begin{aligned} h^{*2} = {} & F_{\text{int}}\frac{L_z}{L_x V} \\ & \times \frac{1}{\frac{3}{8}\mu\frac{p_2^2(\lambda_2)}{p_4(\lambda_2)} + \sigma(\lambda_2 - \lambda_1) + \mu(p_0(\lambda_1) - p_0(\lambda_2))}. \end{aligned} \tag{B19}$$

To estimate the stiffness corresponding to changing the buckling wavelength, we will assume that $h = \gamma h^*$. If we substitute this into Eq. (B18) and calculate the second derivative with respect to γ, then the stiffness of the sample associated with changing the buckling wavelength is

$$Y = \frac{1}{2}\frac{\partial^2 F_T}{\partial\gamma^2}\bigg|_{\gamma=1} = \frac{F_{\text{int}}}{Vh^*L_x}. \tag{B20}$$

If we assume that $B \gg \mu$ so that $\lambda_1 \approx 1$, then this calculation recovers the result obtained in the text by dimensional analysis

$$Y \approx B\sqrt{\sqrt{\frac{K}{B}}\frac{1}{L_x}}f(\lambda), \tag{B21}$$

where $f(\lambda)$ is a function of the deformation applied.

[1] N. A. Clark and R. B. Meyer, Appl. Phys. Lett. **22**, 493 (1973).
[2] S. J. Singer, Phys. Rev. E **62**, 3736 (2000).
[3] R. Ribotta and G. Durand, J. Phys. (France) **38**, 179 (1977).
[4] E. Nishikawa, H. Finkelmann, and H. R. Brand, Macromol. Rapid Commun. **18**, 65 (1997).
[5] E. Nishikawa and H. Finkelmann, Macromol. Chem. Phys. **200**, 312 (1999).
[6] C. M. Spillmann, J. H. Konnert, J. M. Adams, J. R. Deschamps, J. Naciri, and B. R. Ratna, Phys. Rev. E **82**, 031705 (2010).
[7] A. Komp and H. Finkelmann, Macromol. Rapid Commun. **28**, 55 (2007).
[8] D. Kramer and H. Finkelmann, Macromol. Rapid Commun. **28**, 2318 (2007).
[9] W. H. de Jeu, B. I. Ostrovskii, D. Kramer, and H. Finkelmann, Phys. Rev. E **83**, 041703 (2011).
[10] H. Schüring, R. Stannarius, C. Tolksdorf, and R. Zentel, Macromolecules **34**, 3962 (2001).
[11] R. Stannarius, R. Köhler, U. Dietrich, M. Lösche, C. Tolksdorf, and R. Zentel, Phys. Rev. E **65**, 041707 (2002).
[12] R. Stannarius, V. Aksenov, J. Bläsing, A. Krost, M. Rössle, and R. Zentel, Phys. Chem. Chem. Phys. **8**, 2293 (2006).
[13] P. Beyer, E. M. Terentjev, and R. Zentel, Macromol. Rapid Commun. **28**, 1485 (2007).
[14] R. Ishige, K. Osada, H. Tagawa, H. Hiwano, M. Tokita, and J. Wantanabe, Macromolecules **41**, 7566 (2008).
[15] J. M. Adams and M. Warner, Eur. Phys. J. E **16**, 97 (2005).
[16] A. Sánchez-Ferrer and H. Finkelmann, Macromol. Rapid Commun. **32**, 309 (2011).
[17] O. Stenull and T. C. Lubensky, Phys. Rev. E **76**, 011706 (2007).
[18] J. M. Adams and M. Warner, Phys. Rev. E **71**, 021708 (2005).
[19] D. Kramer and H. Finkelmann, Phys. Rev. E **78**, 021704 (2008).
[20] O. Stenull, T. C. Lubensky, J. M. Adams, and M. Warner, Phys. Rev. E **78**, 021705 (2008).
[21] J. M. Adams, M. Warner, O. Stenull, and T. C. Lubensky, Phys. Rev. E **78**, 011703 (2008).
[22] J. Adams, S. Conti, and A. DeSimone, Math. Models Methods Appl. Sci. **18**, 1 (2008).
[23] S. Conti, A. DeSimone, and G. Dolzmann, Phys. Rev. E **66**, 061710 (2002).
[24] S. Conti, A. DeSimone, and G. Dolzmann, J. Mech. Phys. Solids **50**, 1431 (2002).
[25] A. DeSimone and G. Dolzmann, Arch. Ration. Mech. Anal. **161**, 181 (2002).
[26] H. Finkelmann, I. Kundler, E. M. Terentjev, and M. Warner, J. Phys. II (France) **7**, 1059 (1997).
[27] E. R. Zubarev, S. A. Kuptsov, T. I. Yuranova, R. V. Talroze, and H. Finkelmann, Liq. Cryst. **26**, 1531 (1999).
[28] J. M. Adams and M. Warner, Phys. Rev. E **72**, 011703 (2005).
[29] A. W. Brown and J. M. Adams, Phys. Rev. E **85**, 011703 (2012).
[30] J. Adams, S. Conti, and A. DeSimone, Continuum Mech. Thermodyn. **18**, 319 (2007).
[31] M. Warner and E. M. Terentjev, *Liquid Crystal Elastomers* (Oxford University Press, Oxford, 2007).
[32] L. R. G. Treloar, H. G. Hopkins, R. S. Rivlin, and J. M. Ball, Proc. R. Soc. London Ser. A **351**, 301 (1976).
[33] R. T. Deam and S. F. Edwards, Philos. Trans. R. Soc. London Ser. A **280**, 317 (1976).
[34] M. Mooney, J. Appl. Phys. **11**, 582 (1940).
[35] R. S. Rivlin, Philos. Trans. R. Soc. London Ser. A **241**, 379 (1948).
[36] M. Gottlieb and R. J. Gaylord, Macromolecules **20**, 130 (1987).

[37] T. Kawamura, K. Urayama, and S. Kohjiya, Macromolecules **34**, 8252 (2001).
[38] J. Schröder and P. Neff, Int. J. Solids Struct. **40**, 401 (2003).
[39] Abaqus 6.10 User Subroutines Reference Manual 1.1.20 (Dassault Systèmes S.A., Vélizy-Villacoublay, 2010).
[40] J. A. Weiss, B. N. Maker, and S. Govindjee, Comput. Methods Appl. Mech. Eng. **135**, 107 (1996).
[41] M. Kaliske, Comput. Methods Appl. Mech. Eng. **185**, 225 (2000).